Bull Volcanol
DOI 10.1007/s00445-011-0481-0

RESEARCH ARTICLE

Satellite and ground observations of the June 2009 eruption of Sarychev Peak volcano, Matua Island, Central Kuriles

Alexander Rybin · Marina Chibisova · Peter Webley · Torge Steensen · Pavel Izbekov · Christina Neal · Vince Realmuto

Received: 14 July 2010 / Accepted: 19 March 2011

Abstract After 33 years of repose, one of the most active volcanoes of the Kurile island arc—Sarychev Peak on Matua Island in the Central Kuriles—erupted violently on June 11, 2009. The eruption lasted 9 days and stands among the largest of recent historical eruptions in the Kurile Island chain. Satellite monitoring of the eruption, using Moderate Resolution Imaging Spectroradiometer, Meteorological Agency Multifunctional Transport Satellite, and Advanced Very High Resolution Radiometer data, indicated at least 23 separate explosions between 11 and 16 June 2009. Eruptive clouds reached altitudes of generally 8–16 km above sea level (ASL) and in some cases up to 21 km asl. Clouds of volcanic ash and gas stretched to the north and northwest up to 1,500 km and to the southeast for more than 3,000 km. For the first time in recorded history, ash fall occurred on Sakhalin Island and in the northeast sector of the Khabarovsky Region, Russia. Based on satellite image analysis and reconnaissance field studies in the summer of 2009, the eruption produced explosive tephra deposits with an estimated bulk volume of 0.4 km^3. The eruption is considered to have a Volcanic Explosivity Index of 4. Because the volcano is remote, there was minimal risk to people or infrastructure on the ground. Aviation transport, however, was significantly disrupted because of the proximity of air routes to the volcano.

Keywords Sarychev Peak · Kurile Islands · Remote sensing · Petrology · SVERT · Volcanic ash · Sulfur dioxide

Editorial responsibility: A. Harris

A. Rybin · M. Chibisova
Institute of Marine Geology and Geophysics,
Sakhalin Volcanic Eruption Response Team,
Nauki Street,
Yuzhno-Sakhalinsk, Russia 693022

P. Webley · T. Steensen · P. Izbekov
University of Alaska Fairbanks Geophysical Institute,
Alaska Volcano Observatory,
903 Koyukuk Drive,
Fairbanks, AK, USA 99775-7320

C. Neal
US Geological Survey, Alaska Volcano Observatory,
4210 University Dr.,
Anchorage, AK, USA 99508-4664

V. Realmuto
Jet Propulsion Laboratory,
National Aeronautics and Space Administration,
4800 Oak Grove Drive,
Pasadena, CA, USA 91109-8099

P. Webley (✉)
Geophysical Institute/Alaska Volcano Observatory,
University of Alaska Fairbanks,
903 Koyukuk Drive,
Fairbanks, AK 99775-7320, USA
e-mail: pwebley@gi.alaska.edu

Introduction

The 2009 eruption of Sarychev Peak was the most significant explosive eruption from a Kurile Island volcano since the eruption of Alaid Volcano in the northernmost portion of the 1,250-km long volcanic arc in 1981 (Smithsonian Institution 1981a, b). Sarychev Peak on Matua Island in the Central Kuriles (Fig. 1) is remote and unmonitored by ground-based instrumentation; hence, a forecast of the onset of the eruption was not possible. However, the Sakhalin Volcanic Eruption Response Team (SVERT; Rybin et al. 2004) identified and reported on a thermal anomaly and low-level ash output in satellite data 22 h before the main explosive phase began. The ensuing ash clouds drifted primarily to the southeast causing

Published online: 15 May 2011

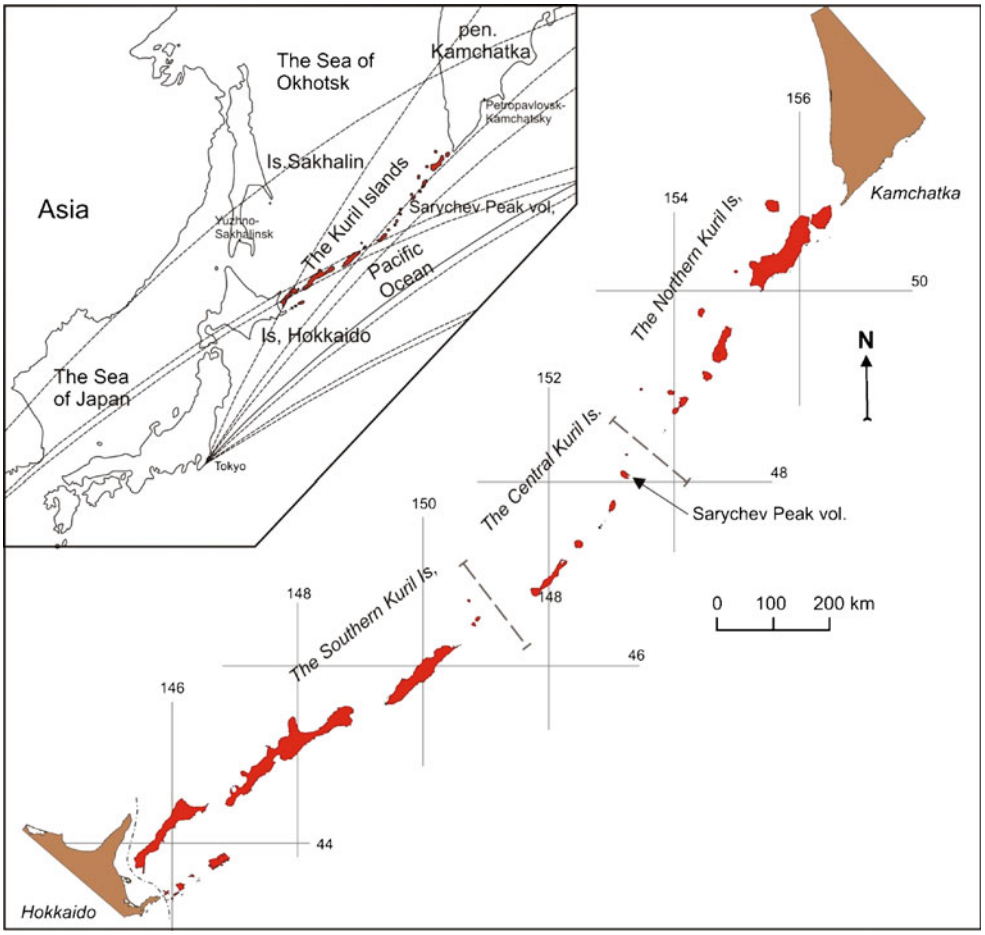

Fig. 1 Map of the Kuril Islands and the zone of the responsibility of the monitoring of the volcanic activity of Sakhalin Volcanic Eruption Response Team (SVERT) and Kamchatka Volcanic Eruption Response Team (KVERT). KVERT issues information for the northernmost Kuriles (Paramushir and Alaid Islands). The remaining Kuriles are monitored by SVERT. Sarychev Peak is located on Matua Island in the north-central Kuriles. *Inset* shows a schematic version of the primary air routes in the vicinity of the northwest Pacific

extensive disruption to international air traffic on routes across the North Pacific (Fig. 1). This paper describes the detailed chronology of events largely based on analysis of satellite imagery, as well as the field observations from a reconnaissance trip in the summer of 2009. Times and dates used are in Coordinated Universal Time (UTC).

Background

Sarychev Peak, historically one of the most active of Kurile volcanoes, is located on remote and currently uninhabited Matua Island in the Central Kuriles (Figs. 1 and 2). Administratively, Matua Island belongs to the North Kurile district of the Sakhalin Region headquartered in Yuzhno-Sakhalinsk on Sakhalin Island. Matua Island is elongated northwest–southeast with dimensions of 12×6 km or 72 km^2 (Fig. 2). Prior to the eruption, the summit elevation of Sarychev Peak was about 1.45 km asl, built atop a Pliocene submarine shield volcano of basaltic and andesitic composition (Gorshkov 1967). Outcrops of this older volcanic structure occur on the southeast and south parts of the island. Also in the southeastern part of the island, lavas and pyroclastic deposits related to a pre-Sarychev caldera, referred to as Matua volcano by Gorshkov (1970), are partially overlain by Sarychev lavas (Fig. 2a); the diameter of the caldera is inferred to be approximately 4 km. According to Gorshkov (1967), the northwestern part of the caldera has been displaced downward along a fault and the modern Sarychev cone has grown within Matua caldera, filling it almost completely. In the southwestern sea cliffs, Gorshkov (1967) states that Matua volcanic sequences composed mainly of andesite and basaltic andesite lava flows are exposed and the upper part of the section exposes pumiceous pyroclastic flows possibly related to Matua caldera formation.

Topography across the southeastern part of the island is rather smooth, comprising vegetated slopes with an average elevation of 30–40 m asl. Rising above the low-lying terrain of this portion of the island is probably a Holocene monogenetic eruptive center, Sopka Kruglaya (Gorshkov 1967) with a diameter of about 400 m and height of 125 m (Fig. 2). Just off the island to the east is the flat, 1×1.4 km, Island of Toporkovyi (Fig. 2). Currently, Sarychev Peak is a typical stratovolcano formed by alternating lava flows and pyroclastic debris, with lavas and pumice being mainly basaltic andesite and rare andesites (Gorshkov 1967; Andreev et al. 1984). Prior to the 2009 eruption, the conical summit of the volcano

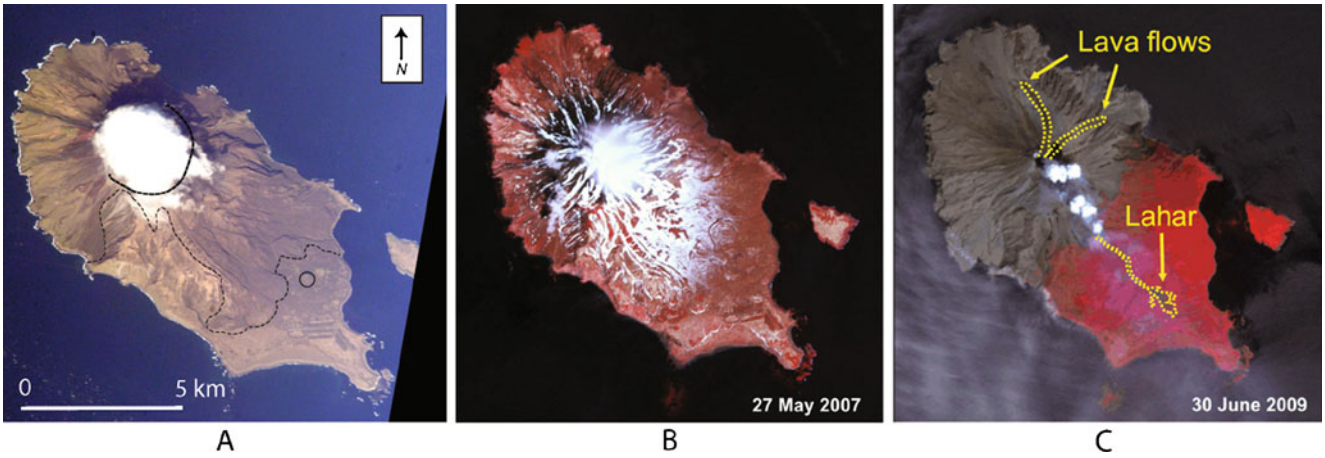

Fig. 2 **a** Sarychev Peak Volcano, Matua Island, 12×6 km. The summit is partially obscured by a cloud cap as seen from the International Space Station. North is towards the top. *Thin dashed line* approximates the extent of modern Sarychev lavas and pyroclastic deposits; *thick dashed line* represents the inferred Matua caldera rim. *Circled* feature in the southeast is a young monogenetic cone (geology modified from Gorshkov 1970). The remains of a World War II Japanese military airfield and base are visible at the *lower right*. Cropped from image ISS005, Roll E, Frame 17795 taken October 18, 2002. Courtesy of the Image Science and Analysis Laboratory, NASA Johnson Space Center, http://eol.jsc.nasa.gov and ASTER daytime thermal infrared (TIR) imagery of Matua Island (12×6 km in dimension) before (**b**) and after (**c**) the eruption. North is at the top. The elongated dark feature extending from the summit to the southeast at C corresponds to a lahar and two lava flows. The southeast portion of the island did not receive much ash fall and was essentially untouched by pyroclastic flows and surges. This region is *red* and correlates to the vegetation left, which was covered to the northeast. Image data courtesy of NASA/GSFC/METI/ERSDAC/JAROS and US/Japan ASTER Science Team

contained a steep walled crater containing a vigorous furmarole field, where Fig. 3 shows fumarolic activity in the summit region after the 1976 eruption. The highest and steepest portion of the crater rim was in the eastern part and was obscured by gas plume in Fig. 3.

Sarychev has been very active in the historic period (here defined as approximately the last 250 years). With at least 10 eruptions occurring since 1760, it is possibly the most historically active volcano in the Kurile chain (Table 1). Eruptions range in estimated size from Volcanic Explosivity Index (VEI, Newhall and Self 1982) 0 to VEI 4.

Fig. 3 Fumarolic activity in the summit crater of Sarychev Peak Volcano as viewed from the crater rim, August 2007. Photo by SA Chirkov, IVS FEB RAS. The 1976 lava flow is at *upper left*. In the center is a lava plug

According to Gorshkov (1967), the 1946 eruption remains one of the strongest Kurile events of the last century and produced both lava flows and pyroclastic flows from Sarychev Peak. Prior to 2009, the most recent activity recorded for Sarychev Peak occurred in the 1980s, but details are scant. The Smithsonian Institution (1987, 1989) states that a fresh lava flow was observed in 1986 and small amounts of ash were observed on the flanks of the volcano in 1989. However, it is likely that the lava flow was in fact the still-warm 1976 flow rather than a new eruptive product.

2009 Eruption chronology

On June 6, 2009, only 5 days before the eruption, a group from the Institute of Marine Geology and Geophysics of Far East Branch of Russian Academy of Sciences (IMGG FEB RAS) visited Matua Island to service permanent Global Positioning System (GPS) stations. During the first 3 days of the eruption, the GPS station moved by ~30 mm northwestwards (towards the crater) and sank by ~40 mm. Before the eruption, there had been no significant shifts (Levin et al. 2010). Members of the team noted strong steaming from the summit crater. On the night (UTC time) of June 11–12, the scientific research ship "George Steller" passed by the island, but according to the chief of the expedition, weather and visibility were poor and there were no obvious signs of increasing unrest (Vladimir Burkanov personal communication 2009).

Table 1 Historical eruptions and other observations of activity at Sarychev Peak

Year	VEI	Details	References
1760	2–3	Great explosive eruption	Gorshkov (1967)
1878–1879	1–2	Quiet effusion of lava on the northeast flank reaching the sea	Gorshkov (1967)
1923	1–2	Explosions with ash and scoria	Gorshkov (1967)
1928	2	Explosive eruption	Gorshkov (1967)
1930	1–2	Great explosive eruption lasting 13 h	Gorshkov (1948, 1967)
1946	3–4	Very strong explosive–effusive eruption with ash clouds to 7 km asl	Glavatskii and Efremov (1948), Siebert and Simkin (2002)
1954	0–1	Weak ash emissions	Gushchenko (1979)
1960	1–2	Explosive eruption, a single event from the upper crater, ash to 4.5 km asl	Shilov (1962), Markhinin (1964), Smithsonian Institution (1976), Siebert and Simkin (2002)
1976	3	Series of explosions destroyed lava dome. Ash/gas cloud extended 300 km north-northeast at 2.5 km asl. Simultaneous lava flows from the summit advanced down the southwest, west, and northwest slopes. Post-eruption, the crater floor was relatively flat and 200 m in diameter	Andreev et al. (1984)
1982–89	0	Intense fumarolic activity at summit crater. Occasional phreatic explosions and lahars	Aerial and ground observations

Volcanic Explosivity Index (VEI) from Simkin and Siebert (1994)

Opening explosions—June 11, 2009

The first sign of volcanic activity at Sarychev volcano was noted by SVERT during its routine daily analysis of the National Aeronautical and Space Administration (NASA) Moderate Resolution Imaging Spectroradiometer (MODIS) data on June 11. Following internal protocol, SVERT sent an email to the Alaska Volcano Observatory (AVO), the Tokyo, Anchorage, and Washington Volcanic Ash Advisory Centers (VAACs), and a variety of other agencies noting a thermal anomaly and a possible weak ash plume in a MODIS image acquired at 0031 UTC. Further satellite data revealed two discrete explosions emitting ash to heights estimated to be below 4 km asl at 0200 and 0700 UTC on June 11 (Fig. 4). These explosions were small relative to later events.

Continued explosions and pyroclastic flow formation—June 12–13, 2009

On June 12, activity intensified suddenly at about 0200 UTC. Our analysis of the satellite data from the next 24 h showed at least eight explosive events sent ash plumes to altitudes of 5–12 km asl (Fig. 4). Poor weather interfered with visual and satellite observations of the volcano. However, based on an analysis of satellite data, the first composite ash cloud from this sequence of events extended up to 350 km southeast of the volcano. The largest explosion during this 24-h period (June 12; 0200 UTC–June 13; 0200 UTC) occurred at 0757 UTC, June 12, and formed a voluminous ash column with a diameter of 35 km and a maximum vertical extent of approximately 12 km asl, as determined using the altitude–temperature method (Kienle and Shaw 1979; Sparks et al. 1997). This method has limitations at the troposphere–stratosphere boundary (as described by Woods and Self 1992) and we have supplemented the analysis with data using the parallax method (referred to in Oppenheimer 1998) to fully resolve the plume heights for ash clouds reaching about the tropopause boundary, here at around 10 km asl. Wind shear during this time sent ash clouds in multiple directions from the east to southeast and backing to the southwest. Beginning at 1457 UTC, another series of explosions of increasing intensity sent an ash cloud to the southeast more than 500 km from the volcano and to the southwest more than 150 km. Also, pyroclastic flows inundated the north and northwestern flanks of the volcanic cone, as seen in the emplacement of pyroclastic density currents as captured in a series of spectacular photographs from the International Space Station (see example in Fig. 5). Based on analysis of the satellite data, the volcano continued to emit ash at a lower level between each discrete explosion.

Between 0130 and 0450 UTC on June 13, three additional explosions sent ash to about 10 km asl (Fig. 4). Ash clouds produced during this period extended to the east and southeast up to 500 km from the volcano. Five hours later at 0930 UTC, another explosion emitted ash to about 10 km asl, where the ash cloud grew to 120 km in width and 200 km in length extending again to the southeast. The largest explosion of the eruption occurred following about 11 h of continuous low level ash emission. At 2130 UTC, a column of ash from this event had reached an estimated

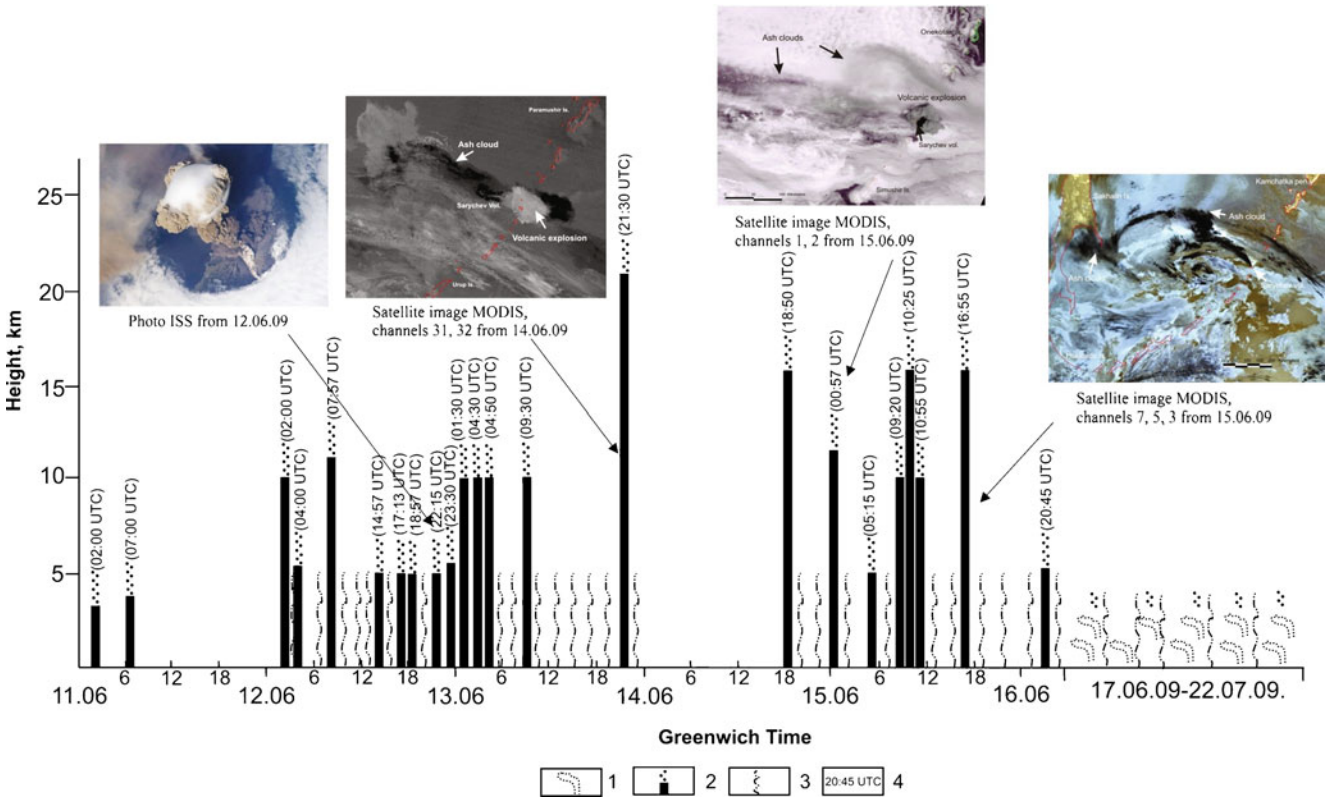

Fig. 4 Summary of satellite observations, inferred explosive events and representative imagery through the eruption, adapted from Levin et al. (2010). Heights of individual ash clouds were determined by using the altitude temperature (Kienle and Shaw 1979; Sparks et al. 1997) and parallax (referred to in Oppenheimer 1998) methods from the MTSAT satellite data and those reported by the Tokyo VAAC. Symbols are as follows: *1* gas–steam emissions, *2* explosions, *3* continuous ash emission, *4* times are reported in Greenwich Time or UTC

21 km asl. Over the next 4 h, a voluminous ash cloud spread to the southeast with lesser amounts to the northwest.

Based on detailed analysis of high-resolution satellite imagery and reports from ground observers Grishin and Melekestsev (2010), as well as Urai and Ishizuka (2009), suggest that during this period the first lava flow formed concurrently with explosive activity. The flow traveled down the northeastern flank of the volcano, reaching its furthest point 2.7 km from the vent by 1500 UTC of June 13 with an average flow rate of 67 mh^{-1} (Grishin and Melekestsev 2010).

Fig. 5 Photograph from the International Space Station of Sarychev in eruption on June 12, 2009. Image courtesy of NASA. North is to *upper right*. Note pyroclastic avalanches descending the north, west, and southeast flanks of the volcano. Airborne ash from a previous explosive event is visible at the *left margin* of the image

Pause in activity and resumed explosions—June 13–16, 2009

Following the large 2130 UTC explosion on June 13, ash emission appeared to cease or diminish significantly at Sarychev Peak for about 13.5 h. It is likely that the effusive activity continued and the second lava flow started its descent down the northern slope during this pause in explosive activity (Grishin et al. 2010). This lull was broken by another large explosion at 1850 UTC on June 14 (a partial evolution of this cloud is illustrated in Fig. 6). The eruption cloud from this event reached an estimated 15 km asl in altitude and rapidly spread east and west (Fig. 6). Over the next 26 h, at least seven additional explosions occurred; lesser events sending ash to 5 km asl and the larger explosions sending ash to 10–16 km asl, using both the altitude–temperature and parallax methods.

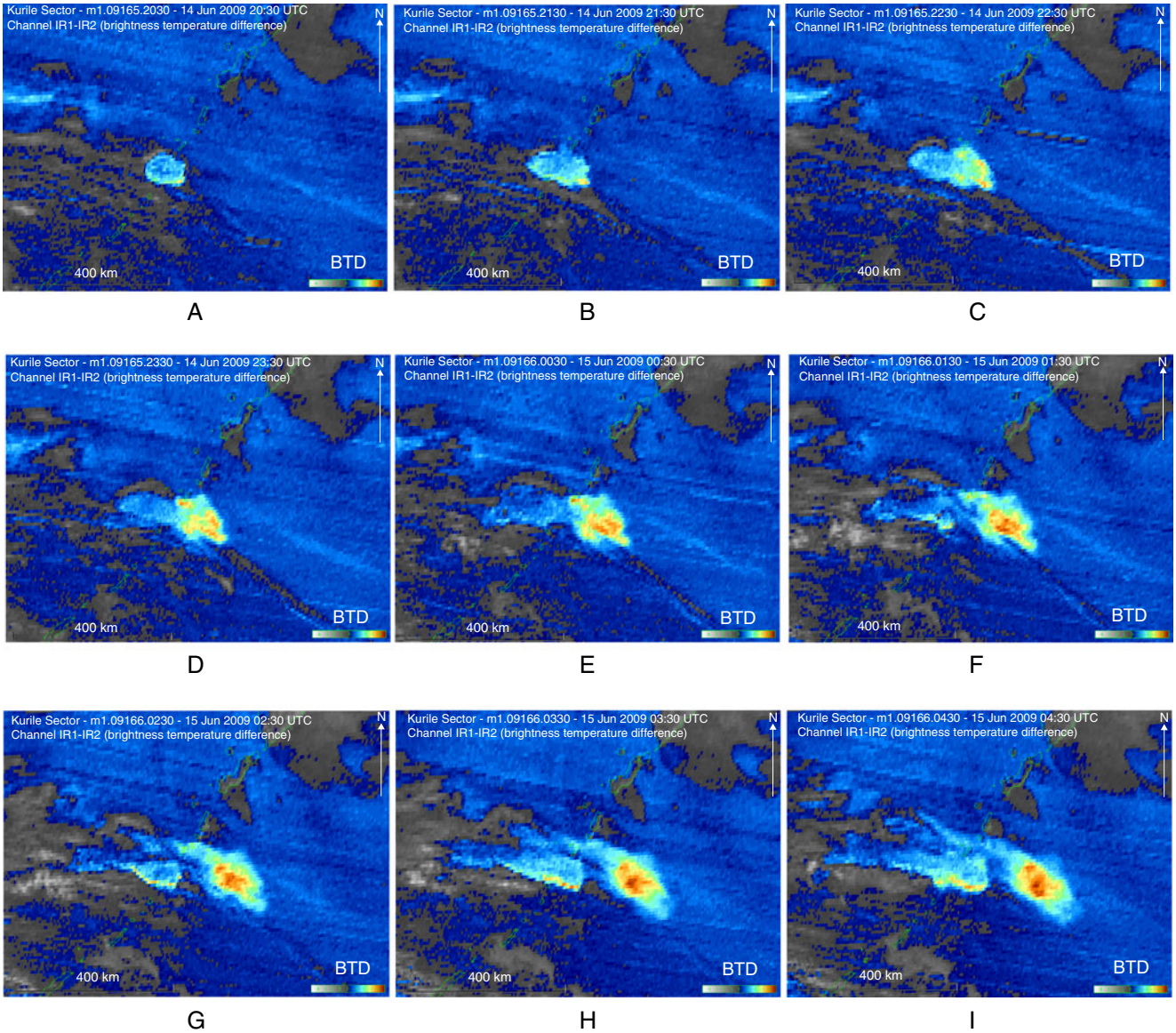

Fig. 6 Sequence of MTSAT scenes showing the development of multiple volcanic clouds over 16.5 h of the most energetic phase of the eruption between June 14 (2030 UTC) and June 15 (0430 UTC). Images display Brightness Temperature Difference (BTD) using reverse absorption technique of Prata (1989a, b). **a** 14 June 2009, 2030 UTC; **b** 14 June 2009, 2130 UTC; **c** 14 June 2009, 2230 UTC; **d** 14 June 2009, 2330 UTC; **e** 15 June 2009, 0030 UTC; **f** 15 June 2009, 0130 UTC; **g** 15 June 2009, 0230 UTC; **h** 15 June, 0330 UTC; and **i** 15 June 2009, 0430 UTC

The resulting ash clouds drifted primarily northwest and southeast for more than 800 km from the volcano.

In between explosive episodes, continuous lower-level emission of ash was detected. The 1655 UTC explosion on June 15 produced the largest ash cloud in terms of aerial extent; prevailing winds to the west and southwest over the Sea of Okhotsk eventually took the ash cloud over Sakhalin Island and the Khabarovsky District west of Sakhalin Island on the Asian mainland (Fig. 1), where a dusting of ash occurred. Using satellite data, the resulting ash plume was estimated to be more than 800 km in length and up to 150 km wide. The eruption continued on June 16 and at 2045 UTC, another explosion sent volcanic ash to about 5 km asl.

Continuous ash emission, weak explosions, fumarolic activity—June 16–19, 2009

The final significant explosion on June 16 was followed by continuous low level emission and the resulting ash cloud traveled primarily to the northwest. Fairly low-level activity—ash and gas emission punctuated by very

weak explosions—continued through June 19, when activity became dominated by the emission of voluminous gas plumes, typically to about 3 km asl, with occasional small amounts of ash.

Post-eruptive fumarolic activity

Strong volcanic emissions, containing mainly steam and gas (Fig. 7) with occasional minor amounts of ash were detected in satellite data and by ground-based observers until October 2009. During this post-eruptive period, thermal anomalies related to strong fumarolic sources and hot pyroclastic debris was also detected at the volcano.

Summary of the eruption chronology

Between June 11 and 19, 2009, we identified 23 discrete explosions from Sarychev Peak Volcano (Fig. 4). These events produced ash clouds of varying sizes and altitudes, with maximum estimated heights ranging from about 3 to 21 km asl. Based on our reconstruction, largely using satellite data, the following stages of activity occured:

Stage 1 Vent opening (June 11, 0200–0730 UTC). Appearance of a large thermal anomaly and weak ash emissions.

Stage 2 First explosive phase (June 12, 0200–June 13, 2130 UTC). Thirteen explosions reaching 5–21 km asl, followed by a lull of about 13.5 h. Effusion of the northeastern lava flow (Grishin and Melekestsev 2010).

Stage 3 Second explosive phase (June 14, 1857 UTC–June 16). Eight explosions up to 16 km asl. Formation of the northern lava flow (Grishin and Melekestsev 2010).

Stage 4 Continuous ash emission (June 17–19). Weak ash emission, ash clouds below 5 km asl.

Fig. 7 Sarychev Peak after the eruption on June 27, 2009. Robust gas and water vapor cloud rises from the summit vent. The green vegetated terrain in the near ground is the southeastern sector of the island that was only minimally impacted by the eruption (see Fig. 2). Photo AV Rybin, IMGG, FEB, RAS

Satellite observations of the eruption clouds

Volcanic ash

Thermal infrared data from the Japanese Meteorological Agency Multifunctional Transport Satellite (MTSAT) sensor were acquired to estimate the mass of the volcanic ash produced from the events between June 14 (2030 UTC) and June 15 (0430 UTC) 2010. The data showed multiple eruptions and evidence of the ash cloud dispersion (Fig. 6). During this period, a brightness temperature difference (BTD) method in the infrared (for MTSAT, IR1 (11 μm)–IR2 (12 μm)), developed by Prata (1989a, b), showed a clear ash signal (Fig. 6). Dry, silicate ash in volcanic clouds/plumes will generate a negative BTD (IR1–IR2<0 for MTSAT), as opposed to meteorological clouds and land/ocean surfaces that produce a near-zero or positive signal. Ash clouds that are detected using one spectral channel in the 10–12 μm range, for MTSAT IR1 or IR2, and that display a high optical depth are classed as spectrally "opaque" (Prata 1989a, b; Webley et al. 2009). This form of ash cloud cannot be detected by the BTD method.

For the reverse absorption or BTD method (Prata 1989a, b; Schneider et al. 1995) to be successful, some portion of the ash cloud needs to be "semi-transparent" which indicates a low optical depth. A negative difference between the two channels generally equates to an ash signal, dominated by dry, fine-grained ash between 1 and 12 μm in effective radius (Rose et al. 2000). Note that the strength of the reverse absorption signal is not directly equivalent to the mass of volcanic ash between the ground and the sensor. To estimate total airborne ash mass, ground surface temperature, cloud top temperature, and refractive indices of the silicate ash are required. Although Simpson et al. (2000; 2001) and Prata et al. (2001) provide some discussions on the limits of this reverse absorption method, in the absence of in situ airborne measurements of volcanic ash concentrations, the reverse absorption method remains the best option for ash cloud detection (Webley et al. 2009). Recent refined algorithms (Pavolonis and Sieglaff 2009) use the reverse absorption features of dry silicate ash at thermal infrared wavelengths to determine volcanic mass loading and hence total mass in the ash cloud. They include additional wavelengths to determine cloud heights and a microphysical model to resolve for the effective particle radius and scattering properties.

A series of eruption clouds from the June 14–15 portion of the 2009 Sarychev Peak eruption have been analyzed for total mass of volcanic ash following the algorithms developed by Wen and Rose (1994). This technique uses BTD data centered at 11 and 12 μm, as well as additional parameters including refractive indices of silicate ash,

ground radiance, cloud top radiance, and particle distribution shapes, to derive plume characteristics, including the total mass, effective particle sizes, and optical depth. However, the de facto BTD threshold for the differentiation between meteorological clouds and volcanic clouds/plumes is not always 0 K. Note an ash cloud is classified when the volcanic plume become detached from the volcano. Figure 6a shows a plume and Fig. 6h shows a cloud to the southeast, along with another plume attached to the volcano.

Using this 0 K threshold would result in the derived volcanic ash mass, in kT, incorporating a large amount of background noise (this can be seen by the dark blue colors as shown in Fig. 6). For this reason, the volcanic mass is calculated at varying reverse absorption thresholds from −0.75 to −3.0 K (Fig. 8). The chosen retrieval parameters are shown in Table 2 and results are listed in Table 3 from the MTSAT data (Fig. 6). In Table 2, the cloud top and cloud base, or surface temperatures, were chosen from analysis of MTSAT satellite data in clear regions not containing the volcanic ash. The refractive index of andesitic ash required in the retrievals came from Pollack et al. (1973) and were used by Wen and Rose (1994) in their analysis of the 1992 Spurr eruption clouds.

An increase in volcanic ash mass within the atmosphere with time can be seen in Fig. 8 and correlates well with the occurrence of the multiple ash explosions shown in the satellite data. With a decreasing threshold for the BTD, this effect becomes less prominent until it disappears at a threshold of −2 K (purple line in Fig. 8). This is a result of the threshold being too constricting and removing large portions of the actual ash cloud from the retrieval. A relatively weak threshold of −0.75 K, on the other hand, likely incorporates a large amount of noise resulting in over estimation of total volcanic ash cloud mass. The similar, but offset, shapes of the time series graphs representing thresholds at −0.75 and −1 K indicate that a lowering in the threshold decreases the contribution of noise to the signal. Using a BTD threshold of −1 K for this period of eruption, the noise in the data has been removed but still retains the volcanic ash cloud signal. This correlates with a mass from about 33 kT at the initial eruption increasing to over 330 kT (0.3 Tg) during the 16.5-h time period analyzed. Note this is similar in size to the Kasatochi 2008 eruption in Alaska, where 0.35–0.5 Tg was detected from satellite infrared ash retrievals (Corradini et al. 2010). Effects of satellite zenith angle relating to the steep zenith angle for geostationary data, as shown by Gu et al. (2005), on the absolute ash mass values could be a factor. However, the overall increase of airborne ash within the time series would still be evident, as the viewing angle stays constant throughout the series.

It is also important to note that the technique used is only sensitive to effective ash particles up to 8 μm in radii (Wen and Rose 1994). The ash retrievals provide the effective radii within each satellite pixel or a measure of the

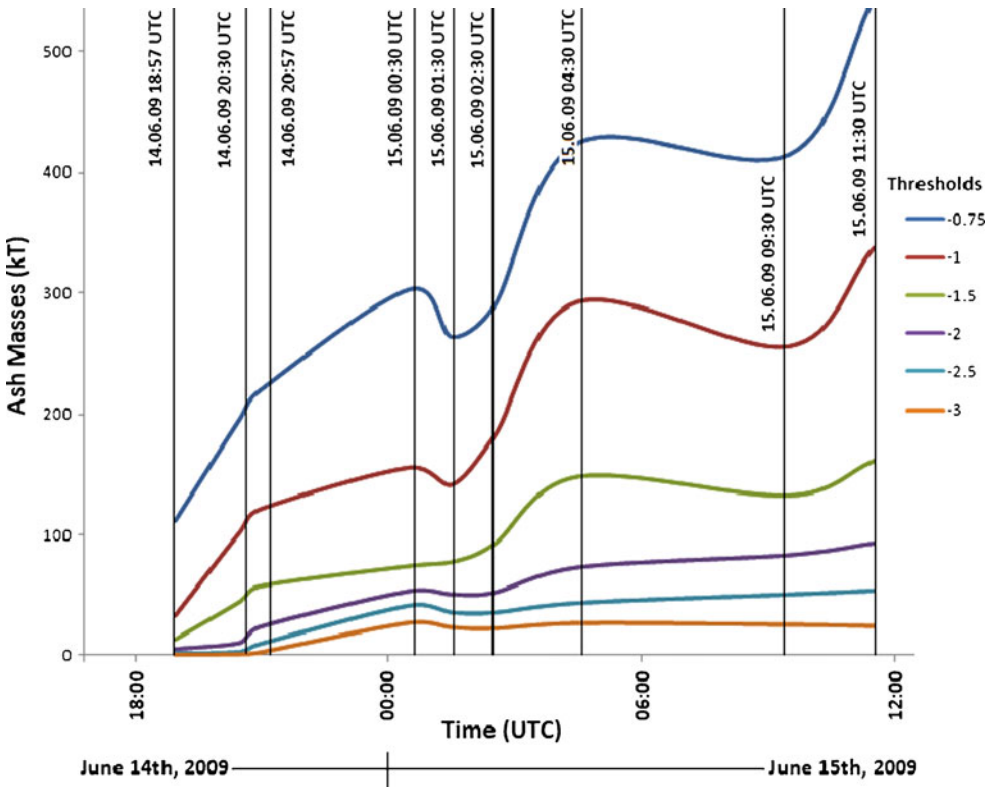

Fig. 8 Visualization of the retrieved ash masses in kilotons (kT) over time for different thresholds. The approximate time of the MTSAT scenes used is marked. The different explosions visible on the images can also be identified in an increase in ash masses here

Table 2 Volcanic ash retrieval parameters used for determination of volcanic ash mass from MTSAT satellite data

Retrieval parameter	Value
Cloud-top temperature (K)	215
Cloud-base (surface) temperature (K)	280
Wavelength of band IR1 (μm)	11.03
Wavelength of band IR2 (μm)	12.02
Aerosol	Andesite (ash)
Specific gravity of volcanic ash	2.6
Refractive index of ambient media	1
Refractive index of ash at IR1	2.14610+0.39891i
Refractive index of ash at IR2	1.82854+0.12953i
Pixel area (km^2)	9
Min effective radius (μm)	0.1
Max effective radius (μm)	30
Number of radii levels	30
Lower radius for ash particle distribution (μm)	0
Upper radius for ash particle distribution (μm)	50
Ash particle radii distribution	Log normal (σ=0.74)

skewness of the size distribution relative to its variance. This is not the absolute radii of the ash particle, but a representation of the particles within the satellite pixel. The effective radius determines how much ash resides in a lognormal distribution range from 0.1 to 100 μm. The larger the effective particle radius, the more particles that will reside in larger size bins, including those size bins greater than 15 μm. If the volcanic ash cloud is dominated with larger particles, the BTD method will detect the ash cloud to be spectrally opaque in the infrared. If the ash cloud is dominated by finer (<50 μm in radii) particles, the cloud will become semi-transparent, as the optical depth is too low and will be detected using the BTD method. Further analysis is required to determine the total mass for the larger and smaller particle size ranges as well as the potential issues of geometric satellite zenith angles. Additional work also includes comparing these volcanic ash masses to total eruptive material, using Sparks et al. (1997) and Mastin et al. (2009) relationships for plume height to eruptive volume.

Table 3 Retrieved ash masses for varying thresholds utilizing the reverse absorption signal and the ash retrieval method developed by Wen and Rose (1994)

	Ash masses (kT) at indicated threshold					
	−0.75	−1.00	−1.50	−2.00	−2.50	−3.00
6/14/09 18:57	111.5	33.1	13.4	5.6	1.6	0.3
6/14/09 20:30	197.0	103.1	45.2	11.0	2.8	0.9
6/14/09 20:57	218.7	121.2	57.6	23.8	9.3	2.2
6/15/09 00:30	302.9	156.1	74.4	53.4	41.5	26.8
6/15/09 01:30	263.3	141.7	77.7	50.7	35.7	22.9
6/15/09 02:30	288.5	181.5	92.3	52.1	35.5	22.0
6/15/09 04:30	424.3	292.9	148.6	72.8	43.6	26.4
6/15/09 09:30	414.5	255.6	132.8	82.9	50.7	25.2
6/15/09 11:30	543.3	337.3	161.6	92.6	53.8	24.1

Sulfur dioxide

Multiple explosions during the 2009 eruption of Sarychev Peak produced significant sulfur dioxide (SO_2), which was detected and tracked downwind for thousands of kilometers. The use of airborne multispectral thermal infrared imagery to map volcanic SO_2 plumes was introduced by Realmuto et al. (1994), and the mapping procedure was refined by Realmuto et al. (1997) and Realmuto and Worden (2000). With the advent of NASA's EOS satellite program, the SO_2 mapping procedure has been applied to MODIS-Terra and MODIS-Aqua data acquired over a variety of volcanoes (e.g., Watson et al. 2004; Kearny et al. 2008; Matiella Novak et al. 2008, and Thomas et al. 2009). Additional SO_2 mapping procedures have been applied to data acquired with the AIRS (e.g., Carn et al. 2005; Prata and Bernardo 2007), Advanced Spaceborne Thermal Emission and Reflection Radiometer (ASTER; e.g., Urai 2004), IASI (Clarisse et al. 2008), SEVIRI (Prata and Keirkmann 2007), and TOVS (Prata et al. 2003) instruments.

Figure 9 shows a mosaic of MODIS data acquired over the Sarychev Peak eruption clouds on June 15 and 16, 2009. The data were processed with the decorrelation stretch (Alley 1996) to enhance spectral contrast. As a result of this processing and compositing, we can recognize the sulfur dioxide clouds, which appear in yellow colors, ash clouds, which appear red/magenta, and ice crystals, which appear blue. Due to this simultaneous depiction of

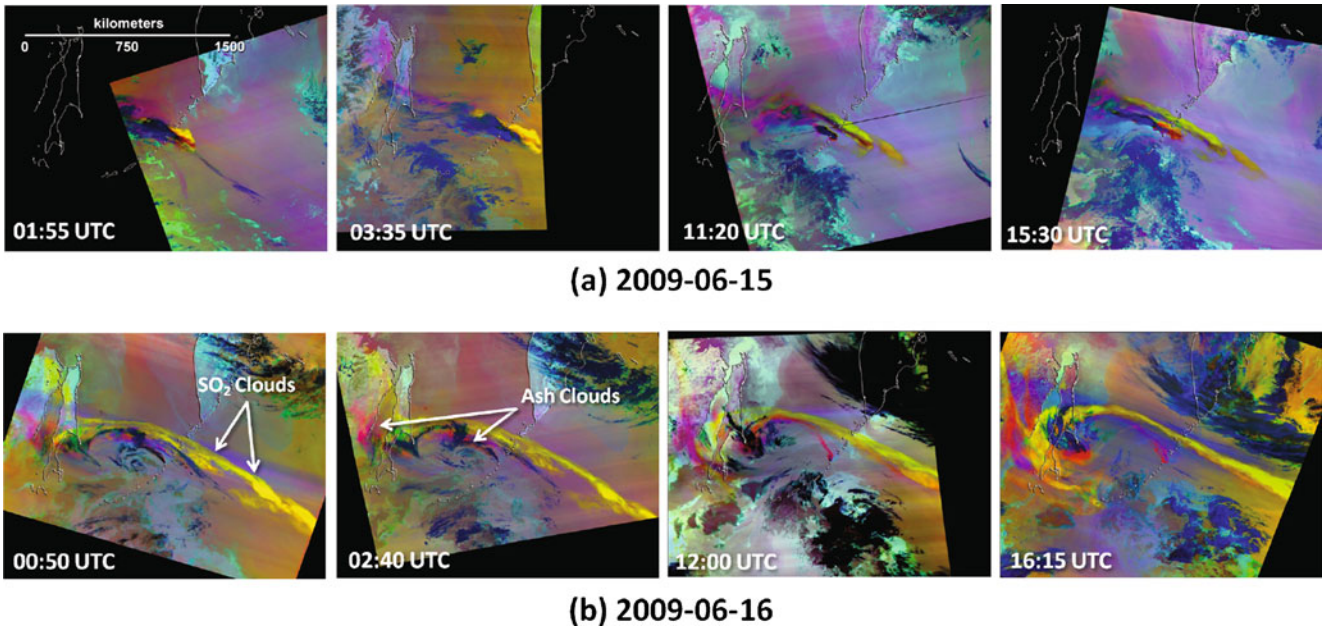

Fig. 9 High altitude SO_2-rich volcanic clouds on June 15 and 16, 2009 as depicted in the MODIS decorrelation stretch. Here, the SO_2 clouds are displayed in *yellow* and the ash clouds are displayed in *red*/*magenta*, with ice crystals are displayed in *blue*

ash and SO_2 clouds, the series of MODIS data (Fig. 9) is a useful complement to the BTD sequence shown in Fig. 6. The MODIS series from June 15 (Fig. 9a) portrayed the accumulation of SO_2 released by sequential explosions of Sarychev Peak into high-altitude clouds, together with the dispersion of ash at lower altitudes. The MODIS series from June 16 (Fig. 9b) highlighted the long-lived nature of the high-altitude SO_2 clouds. The clouds appear to be SO_2 rich from the inception of the explosive episodes on June 15 (Fig. 9a), and the levels of SO_2 appear to remain consistent over the course of June 16, despite the lack of any replenishment by large explosions.

Figure 10 presents NASA ASTER data acquired on June 16, contemporaneous with the MODIS data shown in Fig. 9b. The high spatial resolution of the ASTER data (90 m at nadir) gave a close view of the near-vent region, and allowed us to map SO_2 at the margins of an opaque, ash-rich eruption plume. A comparison of the ASTER and MODIS results (Fig. 10) indicated that the SO_2 concentrations in the high-altitude clouds were roughly similar to

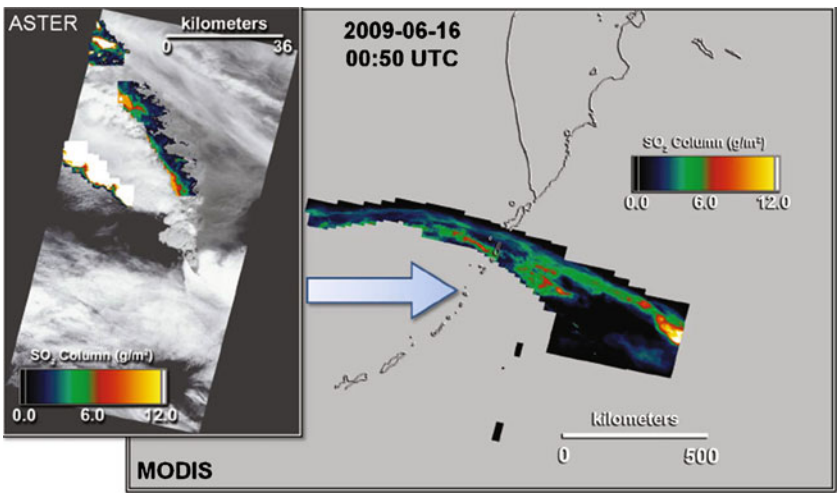

Fig. 10 ASTER and MODIS retrievals of volcanic SO_2-rich clouds on June 16, 2009. The central portion of the eruption plume was opaque in the TIR, so analysis of ASTER data was restricted to the margins of the plume. The highest SO_2 concentrations in the ASTER and MODIS maps are likely due to the presence of ash, which can increase the opacity of the plume and prevent us from deriving an accurate estimate of surface temperature. The ASTER and MODIS results indicate that the SO_2 concentrations in the clouds (MODIS) range between are roughly similar to the concentrations over the vent region (ASTER)

the concentrations near the vent (ASTER). Our estimates of column abundance, the product of SO_2 concentration and plume thickness, ranged between 3 and 6 g/m^2.

We noted that the portions of the high-altitude SO_2 clouds were 18 h old at the time the satellite data were acquired, and we would expect a reduction in SO_2 concentration due to dispersal and conversion to sulfate (SO_4) aerosols. The highest SO_2 concentrations in the ASTER and MODIS maps are likely due to the presence of ash, which increases the opacity of the plume and prevents us from deriving an accurate estimate of surface temperature beneath the clouds (cf. Corradini et al. 2009; Kearney and Watson 2009). In addition, we may be attributing some of SO_2 concentration to SO_4 aerosols. As shown in Fig. 1 of Watson et al. (2004), the spectra of SO_2 and SO_4 are similar in MODIS Channels 29, 31, and 32. As these are the principal channels used in the decorrelation stretch and SO_2 retrieval procedures, it can be difficult to differentiate SO_2 and SO_4 at the spectral resolution of MODIS. Additional work is required to help with this discrimination. Our first-order analysis of the MODIS and ASTER data showed that significant volumes of sulfur dioxide were released during the Sarychev explosions, and the high-altitude clouds retained much of the SO_2 supplied by the explosions

Analysis of the volcanic deposits

A scientific team from IMGG visited Sarychev briefly on June 25 to 28—several days after the end of the explosive phase of the eruption, Fig. 11a shows evidence of hot pyroclastic deposits at the coastline and the volcano steaming from its summit event. Primary products of the eruption included extensive pyroclastic flow deposits and fields of ballistic blocks and tephra-fall deposits, lahars, and two lava flows.

The largest of the juvenile clasts, such as the scoriaceous bombs found atop pyroclastic flow deposits on the slopes of the cone, displayed stretched and fractured textures. Coarse, blocky pyroclastic flow deposits (Fig. 11b, c) covered about 8 km^2 of the island and added about 1–1.5 km^2 to the northeast and southwest coastlines. Some pyroclastic flows consisted of scoriaceous blocks of poorly vesicular material forming steep-fronted lobate deposits (Fig. 11b). Rootless fumaroles were common on the surface of the thicker accumulations of pyroclastic flow deposits: maximum

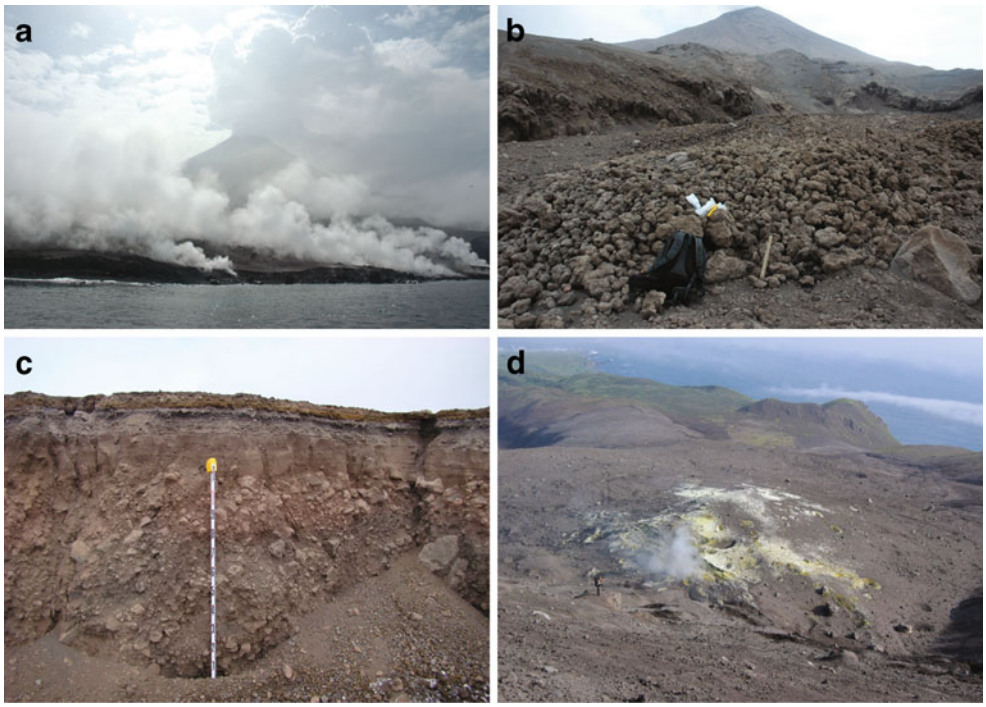

Fig. 11 **a** Sarychev Peak from the north on June 28, 2009. Still-hot pyroclastic deposits at the coastline are producing plumes of water vapor; a robust water-dominated plume emerges from the summit crater and drifts to the south, photo by N Razzhigaeva. **b** Block-rich pyroclastic flow deposit from which the sample P9/2009 was collected (Table 4), photo by AV Rybin taken on June 27, 2009; **c** oxidized, block-rich pyroclastic-flow deposit. Stratified ash and lapilli fall deposits from the late continuous phase of the eruption can be seen atop the pyroclastic flow. Tape measure is extended 1.1 m, photo by N. Razzhigaeva on June 28, 2009; and **d** rootless fumaroles in block-rich pyroclastic flow deposits on the southern flank of Sarychev Peak. Impact craters from rolling volcanic bombs are visible in the *upper left* and *lower right* corners of the photograph, photo by V. Guryanov on June 27, 2009

temperatures of up to 500°C were measured 10–13 days after emplacement (Fig. 11d). These fumaroles were often located near large volcanic bombs carried in pyroclastic avalanches and were visible on the surface of the pyroclastic flow deposits. Additionally from the field observations, mineralization around the fumarolic openings was quite advanced.

ASTER satellite images before and after the eruption showed the distribution of volcanic debris on Matua Island (Fig. 2b, c). A sharp boundary separates the relatively untouched southern portion of the island from the tephra-blanketed northern portion. In the northern part of the island (Fig. 2c), vegetation was buried by up to tens of meters of ash and hot pyroclastic material (Grishin et al. 2010). The southern boundary of this region followed a deep ravine which cuts into the southern slopes of the volcano. Accumulation of hot debris during the eruption caused melting of snow on the slopes of the volcano producing lahars that carried large blocks. Urai and Ishizuka (2009) and Grishin and Melekestsev (2010) both indicate that two linear features were detected on the north–northeast flanks of the volcano. These are new lava flows from the eruptive phase. Additionally, lahars destroyed thick stands of alder and grass on the bottom and sides of the ravine, as described by Grishin et al. (2010). The extent of one lahar deposit southeast of the volcano is shown in Fig. 2c.

Ash fall deposits 1–2 cm thick were reported by various observers and our own sampling collection after the eruption on the islands of Raikoke, Rasshua, Ushishir, Ketoi, Simushir, and the northern part of Urup. In addition, ashfall of up to several millimeters occurred over all of Sakhalin Island and parts of the Khabarovsky Region. Our preliminary estimate of the bulk volume of this eruption is 0.4 km^3. Combining this estimate with observed altitudes of eruption clouds, the 2009 eruption of Sarychev is considered to have a VEI of 4 (Simkin and Siebert 1994; Levin et al. 2009)

Preliminary petrological observations

Fragments of two representative volcanic bombs have been analyzed for bulk chemistry and mineral compositions at the Advanced Instrumentation Laboratory of University of Alaska Fairbanks. The erupted products are basaltic andesites with 54.04–54.41 wt.% SiO_2, 18.23–18.27 wt.% Al_2O_3, and 0.91–0.93 wt.% K_2O (Table 4). The erupted basaltic andesite is crystalline rich, with phenocryst content of nearly 50 vol.%. The mineral assemblage includes plagioclase, clino- and orthopyroxenes, Ti-magnetite, and olivine. The matrix glass shows conspicuous compositional variability (62.26±1.4 wt.% SiO_2) and contains abundant elongate microlites of plagioclase, pyroxenes, and Ti-magnetite (Table 5).

Table 4 Whole rock composition of volcanic features from 2009 Sarychev eruption

Sample	P25/2009	P9/2009
Major elements[a]		
SiO_2	54.04	54.41
TiO_2	0.87	0.88
Al_2O_3	18.27	18.23
Fe_2O_3	9.61	9.74
MnO	0.20	0.20
MgO	4.16	4.12
CaO	9.17	9.1
Na_2O	2.97	2.84
K_2O	0.91	0.93
P_2O_5	0.21	0.21
Sum	100.52	100.76
Sample	P25/2009	P9/2009
Modal analysis[b]		
Glass	48.8	50.3
Pl	30.8	30.5
Cpx	8.4	9.0
Opx	7.8	3.7
Mt	3.8	3.9
Ol	Traces	Traces
Trace elements		
Cr	3	n.d.
V	258	245
Ba	246	325
Zr	72	57
Y	23	22
Sr	491	491
Zn	67	70
Cu	50	46
Ni	7	7

Pl plagioclase, *CPx* clinopyroxene, *OPx* orthopyroxene, *Ol* olivine, and *Mt* magnetite, *n.d.* not detected, *traces* less than 1 wt.%

[a] Major oxides in weight percent with all Fe reported as FeO and concentrations of Ni-Zn (ppm) determined by XRF

[b] Modal analysis is based on mass balance calculations

Plagioclase phenocrysts exhibit the largest degrees of disequilibrium. The oscillatory zoned phenocrysts are exceptionally rare. Their composition is nearly constant at 65.1±1.7 An mol.% and overlaps with composition of outermost sodic rims of the majority of phenocrysts, as well as with composition of microlites (Table 5). Plagioclase phenocrysts with coarsely sieved $An_{76–86}$ cores and 10–80μm wide sodic rims are most common. Their cores contain abundant glass inclusions and voids. At least 5% of all plagioclase phenocrysts contain clear, euhedral calcic cores. The compositional variations of calcic cores

Table 5 Composition of minerals and matrix glass in natural samples

Sample[a]	Matrix glass	Glass incl. in orthopyroxenes	Sodic rims	Microlites	Calcic cores	Clinopyroxene phenocrysts	Clinopyroxene microlites	Orthopyroxene phenocrysts	Orthopyroxene microlites	Olivine	Magnetitie
n	28	3	58	30	71	122	14	63	15	77	14
SiO2	62.26 (1.4)	66.19 (2.15)	52.29 (0.59)	51.74 (1.27)	44.63 (0.62)	51.54 (0.48)	51.58 (0.45)	53.45 (0.46)	53.68 (0.62)	38.96 (0.41)	n.d.
Al2O3	15.48 (1.46)	17.17 (0.33)	30.63 (0.44)	30.86 (1.11)	36.11 (0.45)	2.52 (0.51)	2.52 (0.54)	1.21 (0.22)	1.25 (0.31)	0.01 (0.04)	3.99 (0.18)
TiO2	1.02 (0.31)	0.97 (0.22)	n.a.	n.a.	n.a.	0.52 (0.07)	0.54 (0.08)	0.24 (0.07)	0.24 (0.05)	0.01 (0.03)	9.38 (0.14)
FeOt	6.79 (1.2)	4.28 (2.33)	0.75 (0.08)	0.75 (0.08)	0.53 (0.1)	9.85 (0.57)	10.47 (0.52)	18.87 (1.24)	18.28 (0.46)	20.77 (1.29)	34.82 (0.49)
CaO	5.32 (0.72)	3.47 (0.09)	12.88 (0.4)	13.18 (1.08)	18.72 (0.46)	19.79 (0.38)	19.45 (0.57)	1.64 (0.13)	1.82 (0.15)	0 (0)	47.47 (1.13)
MnO	0.20 (0.06)	0.14 (0.07)	n.a.	n.a.	n.a.	0.42 (0.11)	0.43 (0.13)	0.74 (0.12)	0.74 (0.1)	0.15 (0.03)	n.d.
MgO	1.85 (0.87)	0.83 (0.1)	n.a.	n.a.	n.a.	14.99 (0.39)	14.95 (0.33)	23.82 (0.55)	24.36 (0.51)	0.42 (0.13)	0.50 (0.09)
K2O	1.99 (0.26)	2.32 (0.17)	0.13 (0.02)	0.13 (0.04)	0.02 (0.02)	n.a.	n.a.	n.a.	n.a.	39.62 (1.19)	3.20 (0.2)
Na2O	4.53 (0.38)	3.92 (0.87)	3.72 (0.18)	3.57 (0.56)	0.70 (0.22)	0.29 (0.69)	0.28 (0.05)	0.03 (0.04)	0.02 (0.03)		
Cl	0.16 (0.03)	0.27 (0.03)	n.a.	n.a.	n.a.						
P2O5	0.33 (0.03)	0.27 (0.01)	n.a.	n.a.	n.a.						
Total	100.20 (0.67)	95.96 (0.94)	100.41 (0.55)	100.23 (0.48)	100.72 (0.47)	99.92 (0.69)	100.22 (0.56)	99.99 (0.83)	100.40 (0.7)	99.95 (1.0)	99.38 (1.47)

[a] The average of n analyses (in wt.%) is given with the standard deviation (in brackets). Analyses of glass are normalized to 100 wt.%, however the non-normalized total is reported. Analyses of melt inclusions were re-calculated assuming the presence of water and accounting for the effect of its oxygen on the intensities of all other elements

n.a. not analyzed, *n.d.* not detected

within individual phenocrysts does not exceed 3 An mol.%. There is, however, a conspicuous difference in composition of calcic cores between phenocrysts with $An_{94–96}$ and $An_{89–91}$ cores being the most abundant.

Pyroxenes are euhedral and occur as phenocrysts, microphenocrysts, and microlites. Composition of most phenocrysts and microlites overlaps considerably at $En_{63–69}Fs_{27–33}Wo_{3–4}$ and $En_{41–44}Fs_{16–20}Wo_{38–41}$ for ortho- and clinopyroxenes, correspondingly. Large phenocrysts exhibit subtle compositional zoning with rimward increase of Mg# (Mg/(Mg+Fe), formula units) from 67 to 70 and from 75 to 79 for ortho- and clinopyroxenes, respectively. Magnetites occur as equant phenocrysts, microphenocrysts, and microlites, as well as poikillitic inclusions in both types of pyroxenes. They appear to be texturally and compositionally homogeneous. Olivine crystals comprise less than 1 vol.% of the erupted basaltic andesite. They occur as resorbed $Fo_{72–79}$ phenocrysts and rare poikilitic inclusions in calcic cores of plagioclase phenocrysts. Olivines are commonly surrounded by micro-crystalline pyroxene-magnetite-plagioclase reaction rims.

Based on the compositions of pyroxenes and magnetite, the QUILF model predicts the preeruptive temperature of the 2009 Sarychev magma to have been 1,015± 30°C (Andersen et al. 1993). This overlaps with our temperature estimates of 1,040°C using the two-pyroxene geothermometer of Wells (1977). The deficiency of totals in melt inclusions was 4±1 wt.%, which suggests a preeruptive pressure of 100 MPa based on the water solubility model of Papale et al. (2006). The determined temperature, pressure, and water content are consistent with our P-T-H_2O estimates based on compositions of sodic plagioclases and matrix glass using the plagioclase-melt equilibrium calibration by Lange et al. (2009).

Eruption impacts to aviation and international response

The 2009 Sarychev eruption clearly demonstrated the impact of a Kurile volcanic event due to the proximity of important air traffic routes that are adjacent and downwind of the volcanic arc (Rybin et al. 2004; Neal et al. 2008, 2009). The US Federal Aviation Administration estimated that between June 12 and 15, 2009, 65 reroutes, six diversions, 12 unplanned fuel stops, and two aircraft turned around in flight resulted from the Sarychev ash clouds, costing air carriers approximately $1.8 M (IAVWOPSG/5 2010). Aircraft avoiding ash contaminated air space added between 90 and 120 min of flight time over optimum routings, a significant increase in fuel consumption and associated costs (FAA written communication 2009.)

Furthermore, the location of this eruption required multiple VAACs, Air Route Traffic Control Centers, and Meteorological Watch Offices to issue warning messages, imparting significant challenges to message coordination. Formal warnings to aviation were the immediate responsibility of the Tokyo VAAC and the Aviation Meteorology Center (AMC) in Petropavlovsk, when ash was in Russian air space in the immediate vicinity of Matua Island. For the period of eruption, Tokyo VAAC issued 78 Volcanic Ash Advisories through July 27, 2009. As the ash clouds traveled across VAAC and Flight Information Region

boundaries, formal messages from both the Anchorage VAAC (4) and the Washington VAAC (38) were issued. The Yelizovo AMC in Petropavlovsk produced 68 Significant Metrological Information (SIGMETs) during the eruption and an unknown number of additional SIGMETs were issued by Tokyo and the US Aviation Weather Center.

SVERT, the volcanological authority with eruption reporting responsibility for the southern and central Kuriles, assigned an aviation level of concern color code and provided updates on the ongoing activity via e-mail messages to international aviation and meteorological agencies and local authorities. Lacking any ground-based monitoring equipment, SVERT relied solely on satellite observations to track the eruption. SVERT declared aviation color code RED for the volcano on June 12 and remained there until June 19, when the volcano was downgraded to ORANGE following cessation of major explosive activity. SVERT further downgraded the aviation color code to YELLOW on July 8 and finally to GREEN on October 6. SVERT Information Releases were posted on the IMGG website and mirrored on the website of AVO. AVO staff also conducted telephone call-downs to US aviation and meteorological authorities to assist in disseminating key information about the eruption and path of the ash cloud, also assisting in the monitoring of the region through satellite imagery in their twice daily remote sensing reports.

Discussion

The 2009 eruption of Sarychev Peak volcano was the first large eruption in the Kurile Islands region since 1981 (Smithsonian Institution 1981a, b). It produced a series of ash and sulfur dioxide clouds that reached altitudes as high as 21 km asl and stretched across much of the Northern Pacific Ocean. Discrete tephra explosions and periods of continuous low level ash emission from the summit vent produced widespread ash and lapilli fallout. Coarse pyroclastic avalanches impacted many sectors of the volcano's flanks reaching the sea and extending the shoreline. Lava effusion produced two lobes of lava down the north and northeast flank (Grishin and Melekestsev 2010; Grishin et al. 2010; Urai and Ishizuka 2009). Preliminary petrological observations suggest that the eruption was likely triggered by the influx of basalt into a shallow magma reservoir situated at approximately 3–4 km depth. The high crystallinity of the erupted magma was remarkable and may be one of the factors contributing to the high explosivity of the eruption.

Data presented here shows that the volcanic events introduced significant ash and sulfur dioxide into the troposphere over the North Eastern Pacific. The ability of SVERT, AVO, and the regional VAACs to detect and track activity at Sarychev despite the remoteness of the volcano and lack of ground-based instrumental monitoring demonstrated yet again the critical role of satellite monitoring of volcanoes worldwide. The high temporal resolution of MTSAT data, every 30 min, facilitated the tracking of the ash clouds and generation of formal aviation warning products. The ash plumes and clouds initially tracked to the southeast of the volcano and then later traveled in both northwest and southeasterly directions. Satellite tracking of ash clouds contributes to the refinement of volcanic ash transport models; in particular, the Sarychev eruption of 2009 was another challenging eruption, following on from the Augustine 2006 events (Webley et al. 2010), in producing a series of ash clouds over a short period and thereby testing, model's ability to integrate a series of drifting clouds. Our initial analysis of the ash loading showed that the first portion of the eruption, June 14–15, 2009, produced between around 30 kT of volcanic ash (<50 μm in size), estimated using the BTD and reverse absorption methods, to around 300 kT of volcanic ash by the end of this period. Further analysis is required to examine the particle size distributions of the detected ash clouds to understand which particle sizes dominate the retrievals. Such analysis will assist in determining the total eruptive mass, all particle sizes, from the satellite derived data.

The eruption had significant impacts on aviation in the region over a period of several days and underscored the vulnerability of North Pacific air routes to eruptions in the Russian Far East. Further, with the Tokyo, Anchorage, and Washington VAAC regions of responsibility converging at a "triple point" in the North Pacific, Kurile eruptions present a challenge to information management and coordination systems because ash clouds can quickly extend across VAAC boundaries. The 2009 Sarychev eruption was also the first major volcanic event in the Kurile Islands since the SVERT group was founded in 2003 (Rybin et al. 2004) and provided an important test of the real-time volcanic warning system for Kurile eruptions.

Acknowledgments The authors would like to thank the scientific staff of SVERT and AVO who contributed to the overall response to this significant and dangerous eruption. We acknowledge the hard work and dedication of Japanese, Russian, and American air traffic controllers and aviation meteorologists who, in collaboration with volcanological colleagues, transmit hazard information to the aviation industry in a timely manner. In addition, we would like to thank Rick Wessels and David Schneider of the US Geological Survey for their useful and informative reviews of the manuscript. We highly appreciate constructive peer reviews of Dr. Fred Prata and Dr. Alexander Belousov in the submission process to Bulletin of Volcanology.

References

Alley RE (1996) Algorithm theoretical basis document for decorrelation stretch. Version 2.2

Andersen DJ, Lindsley DH, Davidson PM (1993) QUILF: a PASCAL program to assess equilibria among Fe-Mg-Ti oxides, pyroxenes, olivine, and quartz. Comput Geosci 19:1333–1350

Andreev VN, Shantser AE, Khrenov AP, Okrugin VM, Hechaev VN (1984) Eruption of the volcano Sarychev Peak in 1976. Bull Volcanol Stations 55:35–40

Carn SA, Strow LL, de Souza-Machado S, Edmonds Y, Hannon S (2005) Quantifying tropospheric volcanic emissions with AIRS: the 2002 eruption of Mt. Etna (Italy). Geophys Res Lett 32: L02301. doi:10.1029/2004GL021034

Clarisse L, Coheur PF, Prata AJ, Hurtmans D, Razavi A, Phulpin T, Hadji-Lazaro J, Clerbaux C (2008) Tracking and quantifying volcanic SO2 with IASI, the September 2007 eruption at Jebel at Tair. Atmos Chem Phys 8:7723–7734

Corradini S, Merucci L, Prata AJ (2009) Retrieval of SO_2 from thermal infrared satellite measurements: correction procedures for the effects of ash. Atmos Meas Tech 2:177–191

Corradini S, Merucci L, Prata AJ, Piscini A (2010) Volcanic ash and SO_2 in the 2008 Kasatochi eruption: retrievals comparison from different IR satellite sensors. J Geophys Res. doi:10.1029/2009JD013634

Glavatskii SN, Efremov GK (1948) Eruption of the volcano sarychev peak in the November 1946. Bull Volcanol Stations 15:48–52 (in Russian)

Gorshkov GS (1948) Volcano Sarychev Peak. Bull Volcanol Stations 15:3–7

Gorshkov GS (1967) Volcanism of the Kurile Island arc. M., Nauka, p. 287 (in Russian)

Gorshkov GS (1970) Volcanism and the upper mantle; investigations in the Kurile Island Arc. Plenum Publishing Corp, New York, p 385

Grishin S, Melekestsev IV (2010) Lava flows from the 2009 eruption of Sarychev Peak, the Central Kuriles. Vestnik KRAUNTZ 1: 232–239. Available from: http://www.kscnet.ru/kraesc/2010/2010_15/art19.pdf.

Grishin S, Girina OA, Verechshaga EM, Viter IV (2010) Powerful eruption of Sarychev Peak volcano (Kurile Islands, 2009) and its impact on the plant cover. Vestnik DVO RAN, Vulkanologia i Seismologia, 3:40–50 (in Russian)

Gu YX, Rose WI, Schneider DJ, Bluth GJS, Watson IM (2005) Advantageous GOES IR results for ash mapping at high latitudes: cleveland eruptions 2001. Geophys Res Lett 32: L02305. doi:02310.01029/02004GL02165

Gushchenko II (1979) The eruption of the volcanoes in the world. M.: Nauka, p. 476 (in Russian)

IAVWOPSG/5 (2010) Costs of ash avoidance to US carriers during the eruptions of Redoubt and Sarychev volcanoes in 2009. Available from: http://www.2.icao.int/en/anb/met-aim/met/iavwopsg/IAVWOPSGMeetings/IP7.pdf

Kearney CS, Watson IM (2009) Correcting satellite-based infrared sulfur dioxide retrievals for the presence of silicate ash. J Geophys Res 144:D22208. doi:10.1029/2008JD011407

Kearny CS, Dean K, Realmuto VJ, Watson IM, Dehn J, Prata F (2008) Observations of SO_2 production and transport from Bezymianny volcano, Kamchatka using the Moderate Resolution Infrared Spectroradiometer (MODIS). Int J Remote Sens 29:6647–6665

Kienle J, Shaw GE (1979) Plume dynamics, thermal energy and long distance transport of Vulcanian eruption clouds from Augustine Volcano, Alaska. J Volcanol Geotherm Res 6(1–2):139–164

Lange RA, Frey HM, Hector J (2009) A thermodynamic model for the plagioclase-liquid hygrometer/thermometer. Am Mineral 94 (4):494–506

Levin BW, Rybin AV, Razzhigaeva NG, Vasilenko N, Frolov pervert nurse, Mayor SalyukPa, Zharkov RV, Prytkov AS, Kozlov DN, Chernov AG, Chibisova MV, Guryanov VB, Koroteev IG, Degterev AV (2009) Complex volcano expedition "Sarychev Peak–2009" (The Kuril Island). Bull Far East Branch Russ Acad Sci 6:98–104, in Russian

Levin BW, Rybin AV, Vasilenko NF, Prytkov AS, Chibisova MV, Kogan MG, Steblov GM, Frolov DI (2010) Monitoring of the eruption of the sarychev peak volcano in Matua Island in 2009 (Central Kurile Islands). Dokl Akad Nauk 435(2):255–258 (in Russian)

Markhinin EK (1964) Sarychev volcano. Bull Volcanol Stations 35:44–58 (in Russian)

Mastin LG, Guffanti M, Servranckx R, Webley PW, Barsotti S, Dean K, Denlinger R, Durant A, Ewert JW, Gardner CA, Holliday AC, Neri A, Rose WI, Schneider D, Siebert L, Stunder B, Swanson G, Tupper A, Volentik A, Waythomas CF (2009) A multidisciplinary effort to assign realistic source parameters to model of volcanic ash-cloud transport and dispersion during eruptions. J Volcanol Geotherm Res: Special Issue on Volcanic Ash Clouds, eds. Larry Mastin and Peter Webley 186 (1–2):10–21.

Matiella Novak MA, Watson IM, Delgado-Granados H, Rose WI, Cardenas-Gonzales L, Realmuto VJ (2008) Volcanic emissions from Popocatepetl volcano, Mexico, quantified using Moderate Resolution Imaging Spectroradiometer (MODIS) infrared data: a case study of the December 2000–January 2001 emissions. J Volcanol Geotherm Res 170:76–85

Neal C, Rybin A, Chibisova M, Miller E (2008) Active volcanoes of the Kurile Islands: a reference guide for aviation users: US Geol Surv Open File Report 2008–1162, p. 10

Neal C, Girina O, Senyukov S, Rybin A, Osiensky J, Izbekov P, Ferguson G (2009) Russian eruption warning systems for aviation. Nat Hazards 51:245–262. doi:10.1007/s11069-009-9347-6

Newhall CG, Self S (1982) The Volcanic Explosivity Index (VEI): an estimate of explosive magnitude for historical volcanism. J Geophys Res 87(C2):1231–1238

Oppenheimer C (1998) Volcanological applications of meteorological satellites. Int J Rem Sens 19:2829–286

Papale P, Moretti R, Barbato D (2006) The compositional dependence of the saturation surface of H_2O+CO_2 fluids in silicate melts. Chem Geol 229:78–95

Pavolonis MJ, Sieglaff J (2009) GOES-R Volcanic ash: detection and height. NOAA/NESDIS/STAR GOES-R Advanced Baseline Imager (ABI) Algorithm Theoretical Basis Document, Version 2.0.

Pollack JB, Toon OB, Kane BM (1973) Optical properties of some terrestrial rocks and glasses. Icarus 19(3):72–389

Prata AJ (1989a) Infrared radiative transfer calculations for volcanic ash clouds. Geophys Res Lett 16:1293–1296

Prata AJ (1989b) Observations of volcanic ash clouds in the 10–12 μm window using AVHRR/2 data. Int J Rem Sens 10:751–761

Prata AJ, Bernardo C (2007) Retrieval of volcanic SO_2 column abundance from Atmospheric Infrared Sounder data. J Geophys Res 112:D20204. doi:10.1029/2006JD007955

Prata AJ, Keirkmann J (2007) Simultaneous retrieval of volcanic ash and SO_2 using MSG-SEVIRI measurements. Geophys Res Lett 34:L05813. doi:10.1029/2006GL028691

Prata F, Bluth G, Rose W, Schneider D, Tupper A (2001) Comments on "Failures in detecting volcanic ash from a satellite-based technique". Rem Sens Environ 78:341–346

Prata AJ, Rose WI, Self S, O'Brien D (2003) Global, long-term sulphur dioxide measurements from TOVS data: a new tool for studying explosive volcanism and climate. Volcanism and the Earth's Atmosphere. American Geophysical Union, Washington, DC, pp 77–92

Realmuto VJ, Worden HA (2000) The impact of atmospheric water vapor on the thermal infrared remote sensing of volcanic sulfur dioxide emissions: a case study from the Puu Oo vent of Kilauea Volcano, Hawaii. J Geophys Res 105(B9): 21497–21508

Realmuto VJ, Abrams MJ, Buongiorno MF, Pieri DC (1994) The use of multispectral thermal infrared image data to estimate the sulfur dioxide flux from volcanoes; a case study from Mount Etna, Sicily, July 29, 1986. J Geophys Res B 99:481–488

Realmuto VJ, Sutton AJ, Elias T (1997) Multispectral thermal infrared mapping of sulfur dioxide plumes; a case study from the East Rift Zone of Kilauea Volcano, Hawaii. J Geophys Res B 102:15057–15072

Rose WI, Bluth GJS, Ernst GGJ (2000) Integrating retrievals of volcanic cloud characteristics from satellite remote sensors: a summary. Philos Trans R Soc Lon: A Math Phys Eng Sci 358:1585–1606

Rybin AV, Karagusov YV, Izbekov P, Terentyev NS, Guryanov VB, Neal C, Dean K (2004) Status of monitoring active volcanoes of the Kurile Islands: Present and future: in Proceedings of the Second International Conference on Volcanic Ash and Aviation Safety. Published by the Office of the Federal Coordinator for Meteorological Services and Supporting Research, Session 2:61–66

Schneider DJ, Rose WI, Kelley L (1995) Tracking of 1992 eruption clouds from Crater Peak vent of Mount Spurr Volcano, Alaska, using AVHRR. In Keith TEC (ed) The 1992 eruptions of Crater Peak vent, Mount Spurr Volcano, Alaska, US Geol Surv Bull 2139:27–36

Shilov VN (1962) The eruption of volcano Sarychev Peak in 1960. The book of SakhSRI 12:143–149 (in Russian)

Siebert L, Simkin T (2002) Volcanoes of the World: an Illustrated Catalog of Holocene Volcanoes and their Eruptions. Smithsonian Institution, Global Volcanism Program Digital Information Series, GVP-3. Available from: http://www.volcano.si.edu/world/.

Simkin T, Siebert L (1994) Volcanoes of the world. Geoscience Press, Inc., p. 349

Simpson JJ, Hufford G, Pieri D, Berg J (2000) Failures in detecting volcanic ash from satellite based technique. Rem Sens Environ 72:191–217

Simpson JJ, Hufford GL, Pieri D, Servranckx R, Berg JS, Bauer C (2001) The February 2001 eruption of Mount Cleveland, Alaska: case study of an aviation hazard. Weather Forecast 17:691–704

Smithsonian Institution, (1976) Sarychev. Scientific Event Alert Network Bulletin 1(13)

Smithsonian Institution (1981a) Sarychev Peak. Scientific Event Alert Network Bulletin 6(4)

Smithsonian Institution (1981b) Alaid volcano. Scientific Event Alert Network Bulletin 6(12)

Smithsonian Institution (1987) Sarychev Peak. Scientific Event Alert Network Bulletin 12 (4)

Smithsonian Institution (1989) Sarychev Peak. Scientific Event Alert Network Bulletin 14(3)

Sparks RSJ, Bursik MI, Carey SN, Gilbert JE, Glaze L, Sigurdsson H, Woods AW (1997) Volcanic plumes. Wiley, Chichester, p 589

Thomas HE, Watson IM, Kearney CS, Carn SA, Murray SJ (2009) A multi-sensor comparison of sulphur dioxide emissions from the 2005 eruption of Sierra Negra volcano, Galapagos Islands. Rem Sens Environ 113:1331–1342

Urai M (2004) Sulfur dioxide flux estimation from volcanoes using Advanced Spaceborne Thermal Emission and Reflection Radiometer—a case study of Miyakejima volcano. Jpn J Volcanol Geotherm Res 134:1–13

Urai M, Ishizuka Y (2009) Satellite based observation and interpretation of the 2009 Sarychev Peak eruption on Matua Island of Kurile Islands, Russia. Eos Trans. AGU, 90(52), Fall Meet. Abstract V21B-1984.

Watson IM, Realmuto VJ, Rose WI, Prata AJ, Bluth GJS, Gu Y, Basder CE, Yu T (2004) Thermal infrared remote sensing of volcanic emissions using the Moderate Resolution Imaging Spectroradiometer (MODIS). J Volcanol Geotherm Res 135:75–89

Webley PW, Dehn J, Lovick J, Dean KG, Bailey JE, Valcic L (2009) Near real time volcanic ash cloud detection: experiences from the Alaska Volcano Observatory. J Volcanol Geotherm Res: Special Issue on Volcanic Ash Clouds, eds. Larry Mastin and Peter Webley 186(1–2):79–90

Webley PW, Dean KG, Dehn J, Bailey JE, Peterson R (2010) Volcanic-ash dispersion modeling of the 2006 eruption of Augustine volcano using the Puff model, chapter 21 of Power. JA, Coombs ML, Freymueller JT (eds) The 2006 eruption of Augustine Volcano, Alaska. US Geol Surv Prof Pap 1769:507–526

Wells PRA (1977) Pyroxene thermometry in simple and complex systems. Contrib Mineral Petrol 62:129–139

Wen S, Rose WI (1994) Retrieval of sizes and total masses of particles in volcanic clouds using AVHRR bands 4 and 5. J Geophys Res 99(D3):5421–5431

Woods AW, Self S (1992) Thermal disequilibrium at the top of volcanic clouds and its effects on estimates of the column height. Nat 355:628–630